AUTOMATIC CO-REGISTRATION OF VOLUMETRIC IMAGES BASED ON IMPLANTED FIDUCIAL MARKERS

Martin Koch, Jonathan S. Maltz, Bijumon Gangadharan, Supratik Bose, Himanshu Shukla and Ali R. Bani-Hashemi *

Siemens Medical Solutions (USA) Inc.
Oncology Care Systems Group
4040 Nelson Ave
Concord, CA 94520

Serge J. Belongie

Department of Computer Science
and Engineering
University of California, San Diego
9500 Gilman Drive, Mail Code 0404
La Jolla, CA 92093

ABSTRACT

The accurate delivery of external beam radiation therapy is often facilitated through the implantation of radio-opaque fiducial markers (seeds). Before the delivery of each treatment fraction, seed positions can be determined via volumetric imaging. By registering these seed locations with the corresponding locations in the previously acquired treatment planning CT, it is possible to adjust the patient position or the treatment plan so that seed displacement is accommodated. We present an automatic algorithm that identifies seeds in both planning and pretreatment images and subsequently determines the geometric transformation between the two sets. The algorithm is applied to the imaging series of 10 prostate cancer patients. Each series is comprised of a single multislice planning CT and several megavoltage conebeam CT images obtained immediately prior to a subsequent treatment session. Seed locations were determined for 164 images to within 1mm with an accuracy of $98 \pm 6.3\%$.

***Index Terms*—** image registration, x-ray imaging, pattern recognition

1. INTRODUCTION

The employment of volumetric imaging prior to the delivery of radiation therapy treatment fractions facilitates accurate dose administration by improving the ability to correctly position the patient or to adapt the treatment plan. By co-registering subsequently acquired images with the original planning CT, it is possible to estimate the geometric transformation between anatomic elements. Most contemporary image-guided radiation therapy (IGRT) systems employ registration methods that are based on gray level image matching. In applications such as the imaging of the prostate gland, intrinsically poor contrast between soft tissue structures can lead to inaccurate registration. Often, the influence of bony landmarks dominates other contributions toward the determination of the transformation parameters. This can lead to large inaccuracies, since target structures such as the prostate gland can move by over a centimeter with respect to bony landmarks [1]. Radio-opaque fiducial markers are often implanted into mobile structures such as the prostate gland and lung in order to better identify the displacement and deformation of such organs [2–4]. When such fiducials are available, it makes sense to employ these as landmarks in the co-registration procedure. This is because the presence of fiducials decreases reliance on the skill and anatomical knowledge of the operator, as well as the soft tissue contrast resolution of the imaging modality.

Automatic algorithms were developed previously for the determination of seed displacement using a 2D projection image obtained before treatment delivery, and a digitally reconstructed radiograph (DRR) derived from the planning CT [5]. The algorithm presented here achieves the same objective using 3D datasets. The major advantage of a 3D-to-3D registration is that information from all angular projections is used to determine the seed positions. Consequently, greater accuracy is possible, especially in situations where the presence of more than three markers leads to ambiguity.

2. METHODS

We now describe the proposed algorithm in the context of the imaging and treatment workflow:

1. At the start of the treatment planning process, the patient is imaged using a 3D modality such as x-ray CT or MR. We denote this reference image as Image R.
2. The locations of the fiducial markers are determined manually and saved for later use. We denote the world coordinates of the P markers as $\mathbf{x}_p^R = [x_p \ y_p \ z_p]^T, \ p = 1, 2, \ldots, P$.
3. Before delivery of the nth treatment fraction, the patient is imaged using a 3D modality to yield Image n.
4. The proposed algorithm is used to automatically detect the positions of the fiducial markers within Image n and compute the transformation of these positions with respect to the reference image. The $\mathbf{x}_p^R$ are given as input.

   The registration process proceeds by iterating over three nested loops. The variables k, i and j represent the indices for the thresholding, matching, and grouping loops, respectively. The algorithm proceeds as follows for Image n:

   (a) A volume-of-interest (VOI_n) is defined that constrains the unknown fiducial positions to a feasible volume within the image. This is normally predefined for a specific type of study and is not adjusted on a case-by-case or patient-by-patient basis.

   (b) A thresholding operation is performed to identify voxels in VOI_n that contain highly attenuating material.

*Martin Koch is also with the Department of Pattern Recognition at the University of Erlangen-Nuremburg. Jonathan S. Maltz is also with the Department of Medical Imaging Technology, Berkeley Lab, University of California. This work was supported entirely by Siemens Medical Solutions (USA), Inc.

DOI: 10.1109/ISBI.2008.4541210

These voxel indices are assigned to the set:

$$S_0^k = \{[q,r,s] \mid f[q,r,s] < \gamma \times I_{\max},\ [q,r,s] \in \mathrm{VOI}_n\} \quad (1)$$

where $f[q,r,s]$ is the intensity value of the voxel of Image n at discrete position $[q,r,s]$, $I_{\max}$ is the maximum intensity value in the VOI, and γ is a threshold parameter chosen by the operator.

(c) Connected components analysis [6] is applied to group adjacent points into features. Features whose volume exceeds $V_{\max}$, the maximum expected apparent volume of a seed, are removed from S_0^k.

(d) In order to obtain a reduction in dimensionality and a resulting decrease in computational burden, voxels within close mutual proximity are grouped into the L possibly overlapping sets $g_l, l = 0, 1, \ldots, L$. These sets are collected into the set:

$$G_{ij} = \left\{ g_l \mid g_l \subset S_i^k \right\}, \qquad \bigcup G_{ij} = S_i^k. \quad (2)$$

(e) A matching algorithm is applied that attempts to transform the reference fiducial positions to the positions of the centroids of subsets g_l of the set G_{ij}. The algorithm produces a quality-of-fit metric which is used to select the best match. Let $g_p,\ p = 1, 2, \ldots, P$ be the set of groups that scores the best match. The current set of groups is then updated as:

$$S_{i+1}^k = \bigcup_{p=1}^{P} g_p. \quad (3)$$

(f) Steps d) through e) are repeated until $\left|S_i^k\right| \leq$ UB, where UB is an upper bound of numbers of groups to be used in the matching process. This parameter is chosen by the operator and its value determines the nature of the compromise between processing time and detection accuracy.

(g) At this point, the set S_i^k contains the points $\mathbf{x}_p$ and $P \leq \left|S_i^k\right| \leq$ UB. The transformation parameters are computed to match the $\mathbf{x}_p \in S_i^k$ to the $\mathbf{x}_p^R$. The error of this transformation is denoted ϵ_i.

(h) If $\epsilon_i > \epsilon_{\max}$, we repeat steps b)-g) using a lower value of intensity threshold γ. The parameter $\epsilon_{\max}$ represents the maximum allowed transformation error. This is application dependent and is selected by the operator.

Figure 1 describes the adaptive thresholding and matching process in more detail, as does the exposition below.

2.1. Grouping of points

After elimination of the contribution of large features using connected components analysis, the number of points $\left|S_i^k\right|$ may still be undesirably large for direct application of the matching algorithm. To speed up the matching process, a dynamic grouping process is implemented whereby several single points within close mutual proximity are grouped into the groups g_l. This process is defined by the following pseudocode:

```
D := S_i^k;  l := 1;
for each voxel index in D or until |D| = 0
    find all voxel indices ∈ S_i^k within radius r
    assign voxels indices to g_l
    D := D\g_l
    l := l + 1
end
```

The representative coordinate of a group g_l is computed as the centroid of its points. The maximum distance between two voxels belonging to the same group is smaller than or equal to $2\,r$. Depending on the actual number of groups $|G_{ij}|$, a regrouping may be performed where the proximity radius parameter r is dynamically adjusted to keep the number of groups within the range $P \leq |G_{ij}| \leq$ UB. When such an appropriate group size is attained, the matching algorithm is applied to select the P most relevant groups. These groups are then decomposed into the original points. If more than UB points exist after decomposition, the grouping process is applied, otherwise the points are fed directly to the matching algorithm.

2.2. Matching algorithm

The optimal match is computed by a pattern matching algorithm similar to RANSAC (random sample consensus) [7]. Let D denote the set of points or groups that are fed to the matching algorithm. For the matching of groups and points, we have $D = G_{ij}$ and $D = S_i^k$, respectively.

In each iteration, P elements are randomly chosen out of the set D of candidate matches. Since the order of the points is relevant, the maximum number of iterations necessary to evaluate all matches is $P! \times \binom{|D|}{P}$.

The cost function that is minimized by the matching algorithm is the root mean square of the distance between the transformed source points and the closest points (or group centroids) in the target dataset.

The pseudocode for the matching algorithm is given as follows:

```
for each possible permutation of points or groups
    choose P points x_p out of D
    compute transformation between x_p and x_p^R
    if the matching error ε ≤ ε_+
        break
end
```

The transformation is constrained to consist of rotations around three orthogonal axes and a 3D translation. The RMS distance ϵ between the transformed source points and the current target points is used as the quality metric for the transformation. After evaluating all possible target point combinations, we choose the point set associated with the transformation that produces the smallest error. The iteration over all possible combinations is terminated before an exhaustive search is completed if the error of a transformation is below an operator-defined threshold ϵ_+.

We denote the error obtained upon final application of the matching algorithm, where individual points are considered, as ϵ_{final}.

3. EVALUATION

3.1. Datasets

The algorithm was tested on 164 target datasets obtained from 10 patients. All target datasets were obtained using megavoltage linac beams of Siemens Primus and Oncor radiation therapy linear accelerators. Two different beam configurations were used in the studies. Most images where produced using a conventional 6MV treatment beam. This beam is generated by the action of ≈7MeV electrons on a tungsten target. The resulting photons are filtered using a stainless steel flattening filter. The remaining images were obtained using a prototype imaging system in which ≈4.5MeV electrons impinged on a carbon (diamond) target. No flattening filter was employed. We refer to this beam using the nominal designation “4.5MV”.

The latter studies were obtained over a wide dose range in order to determine the minimum possible useful dose for imaging. As a result, the quality of some of the images is extremely poor. In some

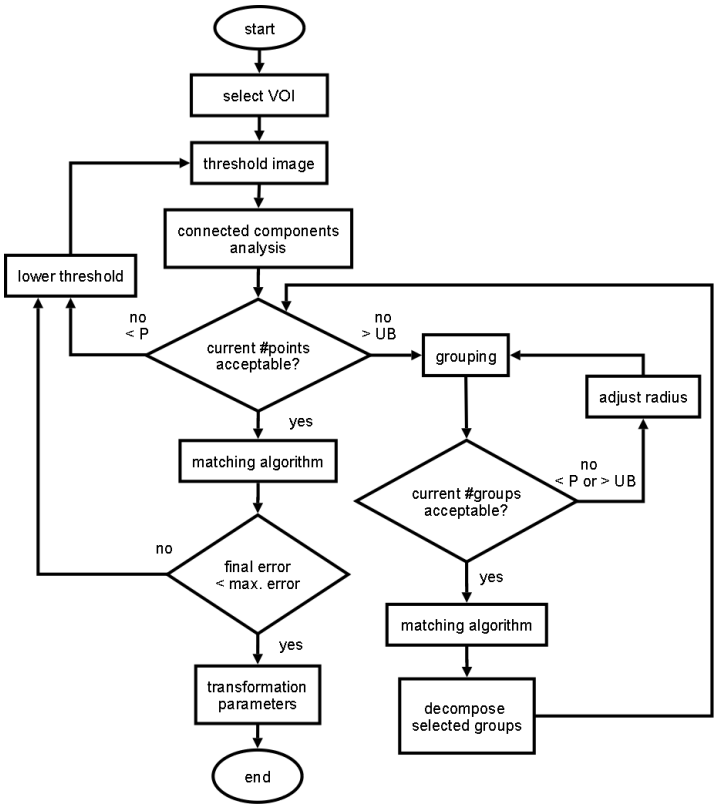

Fig. 1. Algorithm flowchart. Notation: P: number of markers, UB: upper bound used in the matching process.

cases it is not possible for a human observer to identify the fiducial markers.

The images were acquired at the University of California at San Francisco and the Savannah Oncology Center, Savannah, Georgia with the approval of the relevant ethics boards. The algorithm was applied to the data retrospectively and did not influence patient treatment.

A treatment planning CT dataset, obtained using a multislice diagnostic CT system, was obtained for each patient prior to the before-treatment images.

3.2. Specific implementation

A single set of operator-chosen parameters was employed for all datasets examined. We describe these choices below.

3.2.1. Connected components analysis

The actual voxel size of a seed depends on the resolution of the imaging modality, i.e. pixel spacing and slice thickness. For our megavoltage conebeam pre-treatment images we retained as potential seed features only those connected groups having a volume of less than $V_{\max} = 65$ voxels $= 65$ mm^3.

3.2.2. Thresholding

When gold seeds are imaged using megavoltage (MV) beams, their intensity values typically exceed those due to bone by a significant margin. An intensity threshold $\gamma I_{\max}$ that is close to the maximum intensity within the volume of interest is thus appropriate for the thresholding of MV images. We selected $\gamma = 0.85$.

3.2.3. Grouping

The maximum proximity r for group inclusion was initially set to 2.0 mm. Dependent on the actual number of groups $|G_{ij}|$, the radius is either increased or decreased for the regrouping. We set the upper bound on the number of groups UB=15. When more groups are identified than are desired, r is increased by the ratio of the number of current groups and UB. When the number of groups is less than P=3, r is decreased by 1mm for $r \geq$1.5mm and by a factor of $\frac{2}{3}$ otherwise.

3.2.4. Transformation constraints

Rotation was constrained to the angular range between $-\frac{\pi}{8}$ and $\frac{\pi}{8}$. This range accommodates all observed prostate rotations. Translation was not constrained.

3.2.5. Matching

The threshold for early termination ϵ_+ in the grouping stage was set to 0.1 mm (RMS) and the threshold for the final error $\epsilon_{\max}$ to 2.0 mm. These values provide a positioning tolerance of similar magnitude to delivery system and treatment plan tolerances.

4. RESULTS

The results obtained through application of the algorithm to datasets acquired using the 6MV and 4.5MV beams appear in Tables 1 and 2, respectively.

The validated detection rate takes into account only those images that were acquired with doses of 1 cGy or above. The images that were excluded from the calculation of this statistic are marked

Table 1. MV datasets obtained using a 6MV beam

ID	#Datasets	Acquisition time range (days)	CT to 1st MV (days)	#Correct detections	Total correct (%)	Error RMS (mm)	#False detections
c1	41	64	18	41	100 %	0.124 - 0.815	0
c2	25	52	12	25	100 %	0.021 - 1.233	0
c3	3	11	6	3	100 %	0.070 - 0.355	0

Table 2. MV datasets obtained using a 4.5MV beam

ID	#Datasets	Acquisition time range (days)	CT to 1st MV (days)	# Correct detections	#Correct rejections	Total correct (%) validated	Error RMS (mm)	#False detections
i1	8	55	7	7	0	100%	0.075 - 0.248	1*
i2	6	40	15	5	0	100%	0.101 - 0.538	1*
i3	6	22	36	4	1*	80%	0.538 - 1.618	1
i4	4	47	10	4	0	100%	0.033 - 0.240	0
i5	3	3	0	3	0	100%	0.087 - 0.107	0
i6	37	67	0	37	0	100%	0.052 - 0.370	0
i7	31	66	0	29	2	100%	0.075 - 0.890	0

with the superscript "*" in Table 2. We justify this cut-off by observing that the seeds in the <1 cGy images are not visible to human observers.

The average processing time per dataset (mean $\pm$ standard deviation) was 4.7 ± 2.8s for the 6MV studies and 8.1 ± 2.6s for the 4.5MVstudies.

5. DISCUSSION

We described a practical algorithm for the automatic 3D co-registration of metallic fiducial markers and demonstrated its effectiveness through application to a large number of megavoltage CT abdominal datasets.

When applied to images obtained using a commercially-available 6MV imaging system, the algorithm was 100% successful in identifying the fiducial positions (69 studies on 3 patients).

The failure of registration in one study of Series i1 was due to poor image quality. This dataset was produced with dose of 0.3 cGy and was too noisy to allow even manual seed identification.

In Series i2, the matching error in one study was due to a very large amount of prostate motion relative to the reference image. One of the fiducial markers was displaced from the entire volume-of-interest in this case. This case illustrates the importance of operator validation of the final output of the algorithm.

The result obtained for a very low dose (0.6cGy) image in Series i3 represents a true negative. The algorithm was not able to find a match with an acceptably low error and indicated this to the user.

Unexpectedly, application of the algorithm to one higher dose (10cGy) image in Series i3 led to a false positive match. More than five seeds were present within the prostate of this patient. On the day this image was acquired, the patient presented with a highly deformed prostate, probably because of a full bladder and rectum. The presence of this deformation allowed the algorithm to find an acceptable match to an incorrect marker. Selection of the correct match in this case is not straightforward, even for a trained human operator.

In Series i7, two images were rejected due to bad image quality. Both images showed artifacts due to missing tomographic projections, so even manual seed identification was not possible.

The rapid execution time of the algorithm prototype makes it suitable for employment in an image guided radiation therapy workflow.

6. ACKNOWLEDGEMENTS

We would like to thank Dr. Jean Pouliot of the Department of Radiation Oncology at the University of California, San Francisco, and Dr. Morris Geffen at the Savannah Oncology Center of Savannah, Georgia, for providing the patient data for our algorithm evaluation.

7. REFERENCES

[1] E. Vigneault, J. Pouliot, J. Laverdière, J. Roy, and M. Dorion, "Electronic portal imaging device detection of radioopaque markers for the evaluation of prostate position during megavoltage irradiation: a clinical study." *Int J Radiat Oncol Biol Phys*, vol. 37, pp. 205–212, Jan 1997.

[2] A. Nederveen, J. Lagendijk, and P. Hofman, "Detection of fiducial gold markers for automatic on-line megavoltage position verification using a marker extraction kernel (MEK)," *Int J Radiation Oncology Biol Phys*, vol. 47, no. 5, pp. 1435–1442, 2000.

[3] E. J. Harris, H. A. McNair, and P. M. Evans, "Feasibility of fully automated detection of fiducial markers implanted into the prostate using electronic portal imaging: a comparison of methods," *Int J Radiation Oncology Biol Phys*, vol. 66, no. 4, pp. 1263–1270, 2006.

[4] H. Dehnad, A. J. Nederveen, U. A. van der Heide, R. J. A. van Moorselaar, P. Hofman, and J. J. Lagendijk, "Clinical feasibility study for the use of implanted gold seeds in the prostate as reliable positioning markers during megavoltage irradiation," *Radiotherapy and Oncology*, vol. 67, pp. 295–302, 2003.

[5] S. Pouliot, A. Zaccarin, D. Laurendeau, and J. Pouliot, "Automatic detection of three radio-opaque markers for prostate targeting using EPID during external radiation therapy," *IEEE*, 2001.

[6] R. M. Haralick and L. G. Shapiro, *Computer and robot vision*. Reading, Mass.: Addison-Wesley Pub. Co., 1992.

[7] M. A. Fischler and R. C. Bolles, "Random sample consensus: a paradigm for model fitting with applications to image analysis and automated cartography," *Communications of the ACM*, vol. 24, no. 6, 1981.